

Polarization Detection Using Light's Orbital Angular Momentum

Aning Ma, Yuttana Intaravanne, Jin Han, Ruoxing Wang, and Xianzhong Chen*

Polarization detection has been used for a wide variety of applications. A twisted light beam with a helical phase structure carries an orbital angular momentum. The rapid development of optical metasurfaces has enabled practical generation and manipulation of twisted light beams at subwavelength resolution. Herein, a facile metasurface approach is experimentally demonstrated to directly detect the polarization state of light based on the superposition of twisted light beams. The major axis and ellipticity of the polarized light are measured by the interference pattern of two twisted light beams with same topological charges and opposite signs, while the handedness is determined by using topological charges with different values. The subwavelength resolution, ultrathin nature, and compactness render this technology very attractive for diverse applications including optical communications, optical tweezers, and quantum sciences.

biology,^[2] medicine,^[3,4] and microscopy.^[5] Based on the polarization information, one can obtain valuable information about the imaged environment,^[1] e.g., material and tissue properties, surface roughness, shape and texture of reflecting surfaces, the orientation of light emitters, or the optical activity of various materials. A traditional polarization detection system includes many polarization elements, e.g., polarizers, waveplates, polarization modulators, leading to large volume and high cost.^[6] Optical metasurfaces^[7–12] are planar metamaterials that can manipulate the amplitude, phase and polarization^[13] at subwavelength scale, providing unprecedented capability to manipulate light propagation. Optical metasurfaces do not require complicated 3D nanofabrication techniques, but can control light propagation in a desirable manner.^[14,15] Benefiting from the ultrathin nature and high resolution, the use of optical metasurfaces has emerged as a potential candidate for device miniaturization and system integration and a strong candidate for polarization detection. Optical metasurfaces have been used in various polarization detection systems, including circular polarization detection,^[14,16] full polarization measurement,^[17–19] and polarimetric imaging.^[20,21]

1. Introduction

As one of fundamental properties of light, polarization refers to a direction in which an electric component of this light field oscillates. Polarization can be changed upon reflection off a surface or through a polarizer. Polarization has found a wide variety of applications ranging from astronomy and remote sensing^[1] to

tion techniques, but can control light propagation in a desirable manner.^[14,15] Benefiting from the ultrathin nature and high resolution, the use of optical metasurfaces has emerged as a potential candidate for device miniaturization and system integration and a strong candidate for polarization detection. Optical metasurfaces have been used in various polarization detection systems, including circular polarization detection,^[14,16] full polarization measurement,^[17–19] and polarimetric imaging.^[20,21]


In 1992, it was recognized that light beams with a helical phase structure described by $\exp(i\ell\theta)$, where θ is the azimuthal angle and ℓ is the topological charge of optical vortex, carry an orbital angular momentum (OAM) of $\ell\hbar$ per photon.^[22,23] Twisted light beams have been applied in various research fields, including optical communication,^[3] optical trapping,^[24] new forms of imaging systems,^[25–27] nonlinear material,^[28,29] and quantum optics.^[30–32] As a promising candidate, optical metasurfaces have been used to generate various twisted light beams^[33–35] and to control the superpositions of twisted light beams.^[36] However, the utilization of twisted light beam for direct polarization measurement has not been explored. Elliptical polarization is the polarization of electromagnetic radiation such that the tip of the electric field describes an ellipse in any fixed plane intersecting and perpendicular to the direction of light propagation. Any fixed polarization can be described in terms of the shape and orientation of the polarization ellipse, which can be defined by the major axis of polarization, the ellipticity and handedness (clockwise or counterclockwise) (Figure 1). One parameterization of the elliptical figure specifies the orientation angle ψ , defined as the angle between the major axis of the ellipse and the x -axis along with the ellipticity η described by the intensity ratio τ of its left circular polarization (LCP) and right circular polarization (RCP components):

Dr. A. Ma, Y. Intaravanne, Dr. J. Han, R. Wang, Prof. X. Chen
Institute of Photonics and Quantum Sciences
School of Engineering and Physical Sciences
Heriot-Watt University
Edinburgh EH14 4AS, UK
E-mail: x.chen@hw.ac.uk

Dr. A. Ma
School of Information Science and Engineering
Lanzhou University
Lanzhou 730000, China

Dr. J. Han
College of Material Science and Engineering
Kunming University of Science and Technology
Kunming 650093, China

R. Wang
Key Laboratory of In-Fiber Integrated Optics of Ministry of Education
College of Physics and Optoelectronic Engineering
Harbin Engineering University
Harbin 150001, China

 The ORCID identification number(s) for the author(s) of this article can be found under <https://doi.org/10.1002/adom.202000484>.

© 2020 The Authors. Published by WILEY-VCH Verlag GmbH & Co. KGaA, Weinheim. This is an open access article under the terms of the Creative Commons Attribution License, which permits use, distribution and reproduction in any medium, provided the original work is properly cited.

DOI: 10.1002/adom.202000484

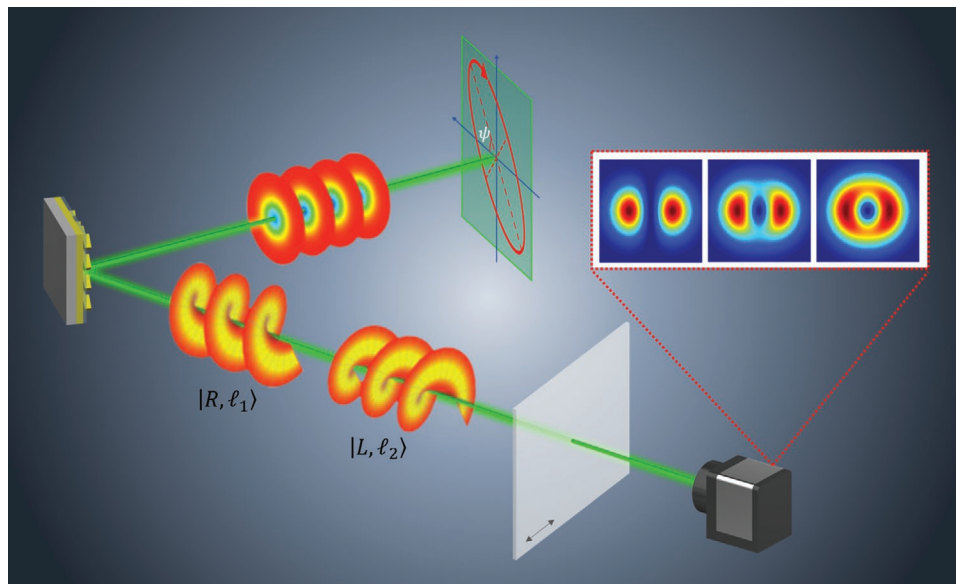


Figure 1. Schematic of the approach for polarization detection using light's OAM. A light beam with unknown polarization shines on a reflective optical metasurface. The emitted light generates the superposition of two OAM states with different topological charges (ℓ_1 and ℓ_2) and opposite circular polarizations, which are described by $|R, \ell_1\rangle$ and $|L, \ell_2\rangle$, where $|R\rangle$ and $|L\rangle$ represent RCP and LCP, respectively. The resultant beam is modulated by passing through an analyzer (linear polarizer) whose transmission axis (denoted by a double-headed arrow) is fixed along x direction. A CCD camera is used to collect the interference patterns of OAM superposition, which is used to measure the polarization state of the incident light.

$\eta = |1 - \sqrt{\tau}| / |1 + \sqrt{\tau}|$ with $\eta = 1$ representing LCP(RCP) light, and $\eta = 0$ representing linear polarization.^[37] In this paper, we propose and experimentally demonstrate a facile metasurface approach to measure the polarization state of an incident light based on the superposition of twisted light beams. The major axis and ellipticity of the polarized light are determined by the interference pattern of two twisted light beams with same topological charges and opposite signs, while the handedness is measured by using topological charges with different values.

Figure 1 shows the schematic of our approach for polarization detection. When a light beam with unknown polarization shines on a reflective optical metasurface, the emitted light generates the superposition of two OAM states, which passes through an analyzer (linear polarizer), whose transmission axis is fixed along x direction. The interference patterns collected by a CCD camera are closely related to the polarization state of the incident light. Based on the analysis of the intensity distribution, the polarization state is directly measured. The direction of the major axis and ellipticity of incident light are measured by the intensity distribution of the superpositions of OAM states with same topological charges and opposite signs. The handedness of incident light is measured by the distance of two maximum intensities of the superpositions of OAM states with different topological charges and opposite signs.

2. Theory and Methods

The superposition of OAM states is based on our recent work that indicates that the incident polarization can be used to arbitrarily control superpositions of OAM states using a single plasmonic metasurface.^[36] The key point of this method is to design a reflective metasurface that can generate a phase profile, which can be used to produce two required OAM beams that

can always meet with each other. Upon the illumination of an incident light with pure circular polarization states (left or right handedness), the two OAM beams can propagate along symmetry-equivalent directions with respect to the axis of incident light. The phase distribution of the metasurface is governed by

$$\Phi(x, y) = \arg(E_1 \exp(i(\ell_1 \theta + \Delta\phi_{\text{off}})) + E_2 \exp(i(\ell_2 \theta - \Delta\phi_{\text{off}}))) \quad (1)$$

where E_1 and E_2 represent the amplitude components of two OAM beams with TCs of ℓ_1 and ℓ_2 , respectively. θ is the azimuthal angle and $\Delta\phi_{\text{off}}$ is the phase difference between neighboring pixels to generate a phase gradient along the x direction, which can introduce off-axis deflection for the OAM mode of interest. To generate the off-axis reflection, the additional phase difference between neighboring pixels of the sample along the direction is $\pi/5$, resulting in a reflection angle of 12.2° at the incident wavelength of 650 nm. It is worth mentioning that the off-axis design can avoid the disturbance of the nonconverted part.

To maintain high efficiency, we use reflective metasurfaces to develop the designed metasurface devices. The general idea is to combine the advantages of both a metallic metamaterial and a dielectric interlayer, which can construct a broadband and highly efficient metasurface, in which the intrinsic dispersion of the metallic nanorods is cancelled out by the thickness-dependent dispersion of the SiO_2 layer. The triple layer structure functions like a Fabry–Perot-like cavity, where the SiO_2 spacer in the middle corresponds to the cavity length. Nanorods along with the spacer and the background layer function as a reflective-type half waveplate,^[38–40] leading to the high efficiency. The theoretical conversion efficiency versus wavelength is provided in the Section S1 (Supporting Information). Fabrication details are provided in the Experimental Section and Section S2 (Supporting Information).

An arbitrary polarization state is the superposition of orthogonal circular polarizations. For example, an incident light beam with linear polarization (LP) along a direction angle α with respect to the x -axis can be decomposed into two equal-weighted RCP and LCP components with a phase difference, which can be described by $e^{i\alpha}|R, -\ell_1\rangle + e^{-i\alpha}|L, \ell_2\rangle$, where $|R\rangle$ and $|L\rangle$ represent RCP and LCP, respectively. When a LP light shines on the metasurface, the superposition of OAM states with $\ell = 1$ and $\ell = -1$ is generated since a linearly polarized light beam can be decomposed into OAM beams with equal weight and opposite topological charges. The superimposed mode can be characterized by passing through a linear analyzer and forming an angle γ with respect to the horizontal axis (x -axis). The Jones matrix of the analyzer has the form^[36]

$$\begin{bmatrix} \cos^2 \gamma & \sin \gamma \cos \gamma \\ \sin \gamma \cos \gamma & \sin^2 \gamma \end{bmatrix} \quad (2)$$

The transmitted intensity profile can be expressed by $E = \frac{1}{2}[1 + \cos^2(\ell\theta + \alpha + \gamma)]$.

For two twisted light beams with same topological charges and opposite signs, the transmitted intensity values are maximum at the azimuth angles $\theta_{\max} = \frac{n\pi - \alpha - \gamma}{|\ell|}$ ($n = 0, 1, \dots, |2\ell| - 1$), leading to $|2\ell|$ lobes. For $|\ell| = 1$ and the analyzer with a fixed direction along the x -axis ($\gamma = 0$), the angle between the major axis and x -axis is $\psi = \theta_{\max} = -\alpha$. Here, θ_{\max} is the angle between the line through the two maximum intensity points and x axis. Since the type of metasurface in this work is reflective, so $\psi = \theta_{\max} = \alpha$ for $\gamma = 0$ and $|\ell| = 1$. The modulated intensity patterns (bright region and dark region) can be used to determine the major axis of the ellipse. There exists a dark region (gap) between neighboring bright petals. If the incident light is elliptically polarized, the darkest region will become brighter in

comparison with LP, indicating this property can be used to determine the ellipticity of the polarized light. To measure the handedness of the polarized light, we use the superposition of two twisted light beam with different topological charges, which can produce OAM beams with different diameters. The handedness of the ellipse is determined by the dominated doughnut shape (brighter) with predesigned handedness.

3. Results

As a proof of concept, we design a metasurface to measure the major axis and the ellipticity of the incident polarization based on the superpositions of OAM states with $\ell = 1$ and $\ell = -1$. **Figure 2a** shows the scanning electron microscopy (SEM) image of fabricated metasurface, which is used to determine the major axis and ellipticity of the elliptically polarized light. **Figure 2b** is the schematic of the experimental setup. To characterize the performance of the metasurfaces, a tunable laser source (NKT-SuperK EXTREME) is used to generate the desired laser beam with various polarization states after passing through a linear polarizer and a quarter-wave plate (QWP) in front of the sample. Details for the generation of polarization states are provided in Section S2 (Supporting Information). An objective with a magnification of 10 \times is used to expand the image for visualization with a CCD camera. The superimposed mode is collected by a CCD camera after passing through an analyzer whose transmission axis is fixed along x -direction.

Figure 3a shows the simulated superpositions of OAM states with $\ell = 1$ and $\ell = -1$ under the illumination of a linearly polarized beam. The transmission axes of polarizer and analyzer are 45 $^\circ$ and 0 $^\circ$ with respect to x -axis, respectively. **Figure 3b** is the experimentally measured superpositions of OAM states. The image contains 460 \times 460 pixels. The green circle in **Figure 3b** has a radius r around the center of the figure. The radius r is

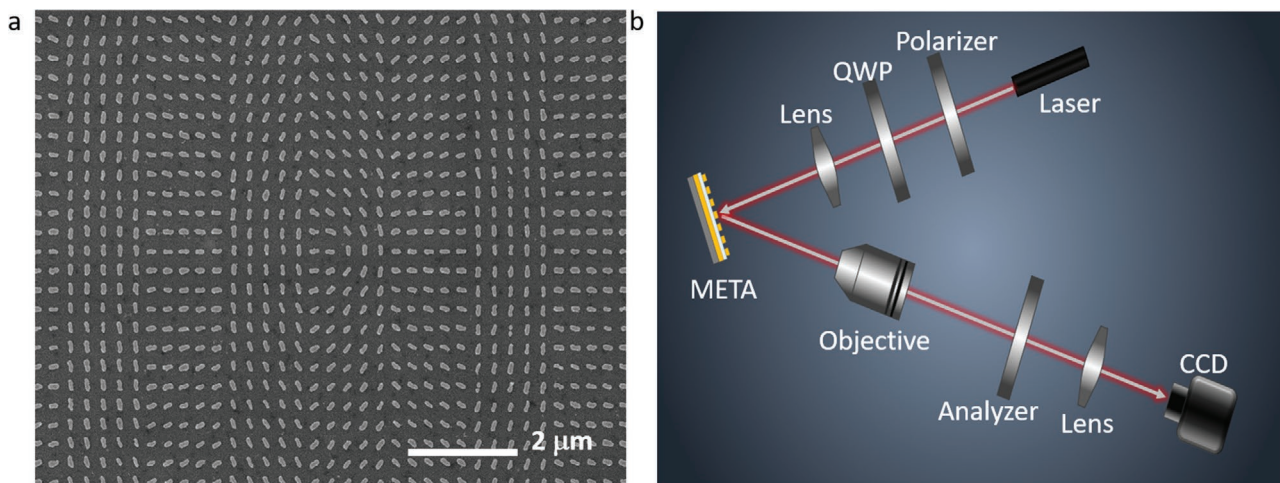


Figure 2. Scanning electron microscopy (SEM) image of the fabricated sample and schematic of the experimental setup. a) SEM image of part of the fabricated metasurface. The reflective optical metasurface consists of gold nanorods with spatially variant orientation, a gold film and a SiO₂ layer sandwiched between them. Each nanorod represents a phase pixel with a size of 300 \times 300 nm². b) The incident light with various polarization states is obtained by controlling the angle between the transmission axis of the polarizer and the fast axis of the quarter wave plate. The incident light impinges normally onto the metasurface and the emitted light is collected by an objective with a magnification of 10 \times objective. The transmission axis of the analyzer is fixed along the x direction.

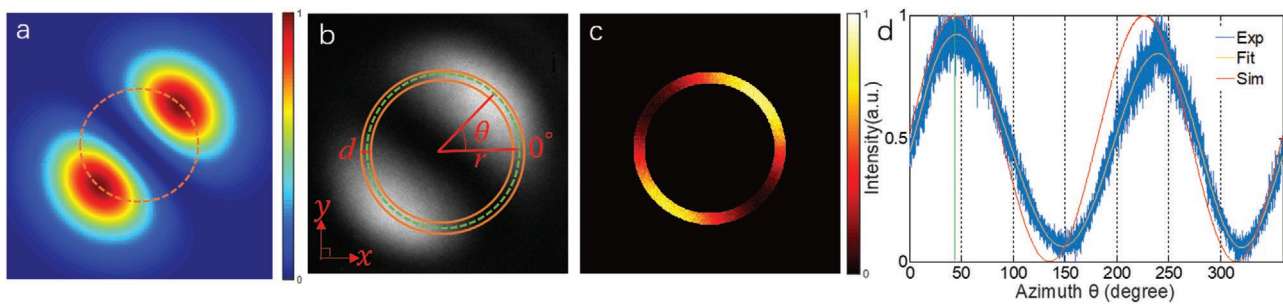


Figure 3. Measurement of major axis of the polarization state. a) Numerically calculated superpositions of OAM states with $\ell = 1$ and $\ell = -1$. The transmission axes of polarizer and analyzer are $\pi/4$ and 0 with respect to x -axis, respectively. The orange dash circle passes through the two maximum intensity points. b) The corresponding experimental result. The image contains 460×460 pixels. The green dash circle has a radius r around the center of the figure. The radius r is determined by distance between the center (the zero intensity) and the maximum intensity. To improve the signal to noise ratio, the intensities in the ring region at each azimuth angle are considered, as schematically illustrated by the orange ring region. The width d of the orange ring is 20 pixels. c) The intensity distribution along the orange ring is extracted based on experimental result, as shown in (b). d) The relation between light intensity distribution in (c) and the azimuth angle. The experimental, fitted and simulated results are in blue, yellow, and red colors. The yellow color represents the 10th polynomial fitting curve of experimental data.

determined by distance between the center (the zero intensity) and the maximum intensity. To enhance the signal to noise ratio, the intensities in the ring region at each azimuth angle θ are considered, as schematically illustrated by the orange ring region in Figure 3b. The width d of the orange ring is 20 pixels. The intensity distribution along the orange ring is extracted based on experimental result, as shown in Figure 3c. By integrating the intensity over the ring width at each azimuth angle θ ranging from 0° to 360° , the corresponding intensity distribution along the ring is obtained (shown by the blue curve in Figure 3d). Although there are many oscillations induced by the noise, which can be improved by using fitted curve using 10th polynomial (denoted by the yellow color), as shown in Figure 3d. In comparison with experimental result, the corresponding simulation result is given in red curve (Figure 3d). Both simulation and experiment have a maximum value at 45° , indicating there is a good agreement between them. To further confirm the validity of this approach, we measured various linear polarization states with different major axes by rotating the transmission axis of the polarizer, while the transmission axis of analyzer is fixed along the horizontal direction. **Figure 4** shows numerically calculated and experimentally observed superpositions of OAM states with $\ell = 1$ and $\ell = -1$ when the rotation angles of the polarizer are 0° , 45° , 90° , and -45° , respectively. Figure 4d presents the simulation (red curves) and experimental results (The blue color represents the experimental data and the yellow color represents the 10th polynomial fitting curve of experimental data), which are normalized intensity distributions as a function of azimuth angle θ , respectively. Because our proposed metasurface is a reflective type, the green vertical line points to the first maximum intensity, whose θ_{\max} just corresponds to the major axis $\psi = \theta_{\max} = \alpha$ of incident linearly polarized light. The polarization direction of the incident linearly polarized light and the direction of the polarizer's transmission axis in front of the CCD camera are respectively denoted by the red and blue double-headed arrows in the first row of figures. The experimental results at other wavelengths are provided in Section S3 (Supporting Information). As we expect, the predesigned major axes of the polarization states agree well with the measured values.

The ellipticity of the incident polarization state can be determined by comparing the intensity of minimum and maximum from the images. **Figure 5a,b** shows the simulation and experimental results of the intensity distribution for a typical polarization state of the incident light, respectively. The experimentally obtained intensity distribution for the superpositions of OAM states with $\ell = 1$ and $\ell = -1$ is processed by the software ImageJ. The spots A and B on the circle represent the two minimum intensity points in the simulation results, while C and D represent two maximum intensity points in simulation results. The minimum intensity spots A' and B' on the circle are denoted by $I_{A'}$ and $I_{B'}$ and the maximum intensity spots C' and D' are denoted by $I_{C'}$ and $I_{D'}$ in experimental results. In order to decrease error, the ellipticity η of the incident light can be calculated by the intensity ratio of minimum intensity and maximum intensity, that is $\eta = \sqrt{(I_{A'} + I_{B'})/2} / \sqrt{(I_{C'} + I_{D'})/2}$. $\eta = 1$ and $\eta = 0$ correspond to CP and LP, respectively. Figure 5c shows the simulation and experimental results of the ellipticity for the incident light with various polarization states, which are realized by rotating the transmission axis of the polarizer with the angle $\alpha = 0^\circ, 10^\circ, 20^\circ, 30^\circ, 40^\circ, 45^\circ, 50^\circ, 60^\circ, 70^\circ, 80^\circ, 90^\circ$ while the fast-axis of QWP and the transmission axis of analyzer are fixed along x direction. The experimental results of the light intensity distribution at the above angles are given in the insets of the figure. A clear dark boundary line between two petals and a doughnut shape are observed at $\alpha = 0^\circ$ (linear polarization along x axis) and $\alpha = 45^\circ$ (circular polarization), respectively. The two petals are located at the top and bottom at $\alpha = 90^\circ$ (linear polarization along x axis). The two petals are gradually joined with each other with the increase of the angle from 0° to 45° , which is the inverse process for the range from 45° to 90° . The relative error between the experiment and simulation ranges from 1.1% to 5.57%. As we can see from the Figure 5c, the experimental data (blue triangle) and simulation data (black line) agree very well with each other. The slight difference between experiment and simulation is due to the imperfection of the sample and measurement error. The details of the simulation and experimental results of the ellipticity for the incident light with various polarization states are available in Section S3 (Supporting Information).

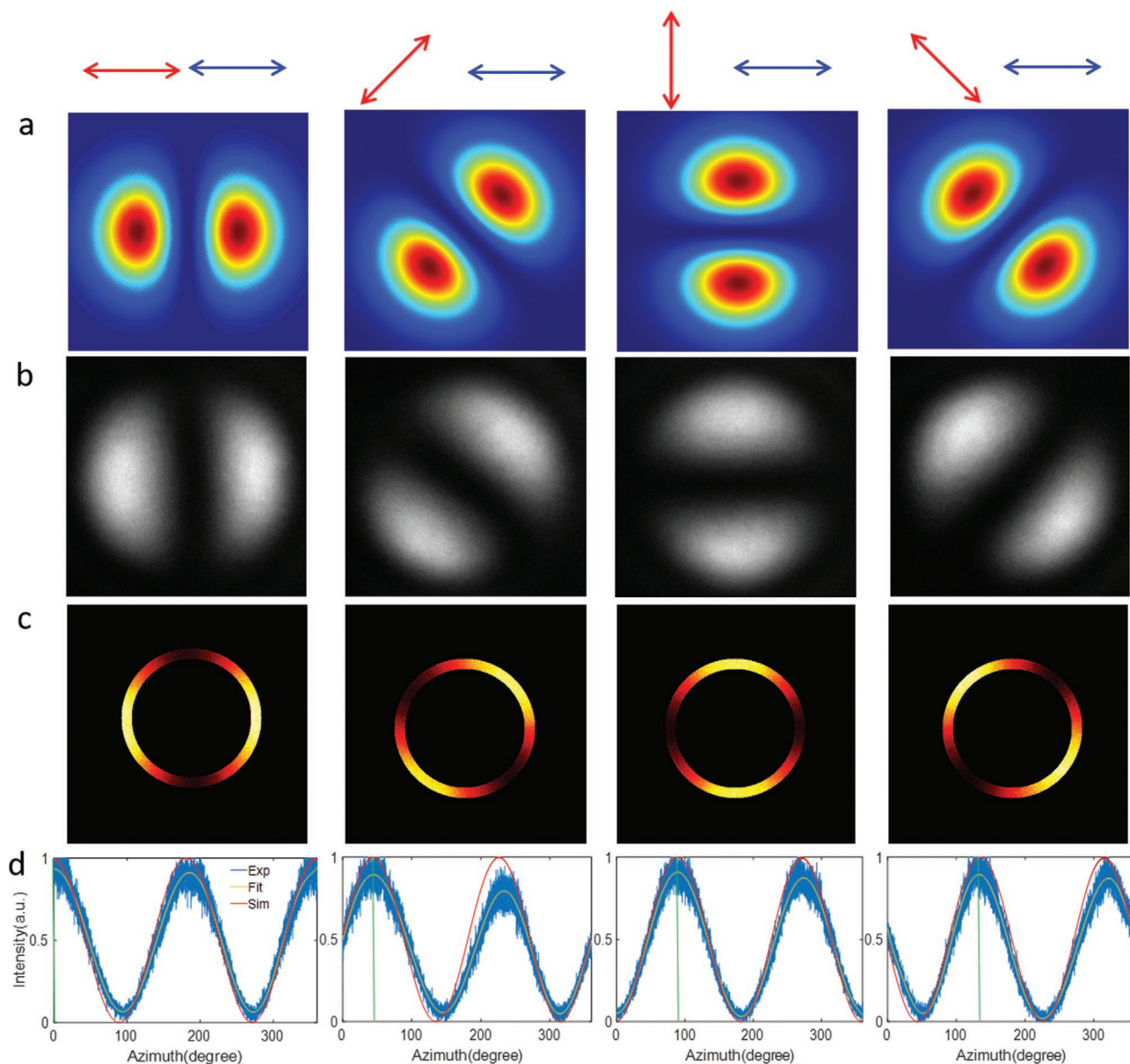


Figure 4. Numerically calculated and experimentally obtained results for the measurement of major axis. a) Simulation results for the superpositions of OAM states with $\ell = 1$ and $\ell = -1$ when the rotation angles of the polarizer are 0° , 45° , 90° , and -45° , respectively. The polarization direction of the incident linearly polarized light and the direction of the polarizer's transmission axis in front of the CCD camera are respectively denoted by the red and blue double-headed arrows. b) Experimental results. c) The intensity distributions along the orange ring shown in Figure 3b. d) The relation between light intensity distribution in (c) and the azimuth angle.

In order to determine the handedness of incident polarized light, we fabricate a metasurface that can realize the superpositions of OAM states with $\ell = 1$ and $\ell = -3$. Upon the illumination of LCP light, the doughnut shape has a smaller radius (corresponding to $\ell = 1$), which will become bigger (corresponding to $\ell = -3$) when the polarization state of the incident light is RCP. Thus, we can tell the handedness of the incident light by comparing the light intensity on the two light rings. To facilitate data analysis, we choose light intensity profile along a rectangle region (edge marked the orange line) with a width of 10 pixels passing through the center of the superposed mode. The orange dash line in the numerical

figure is the vertical center of light intensity distribution. We extract the 600×600 pixels of the center of image. The handedness of incident polarized light is determined by the distance between two peak intensities. The normalized intensity profiles of numerically calculated and experimentally observed superpositions of OAM states with $\ell = 1$ and $\ell = -3$ are given in Figure 6. To confirm the proposed idea, the incident light with various polarization states is used to evaluate the performance of the fabricated sample. The two figures at the bottom are the polarization profiles of normalized intensity for the linear polarization, and the distance between two green vertical dash lines is about 300 pixels. The distances between two green

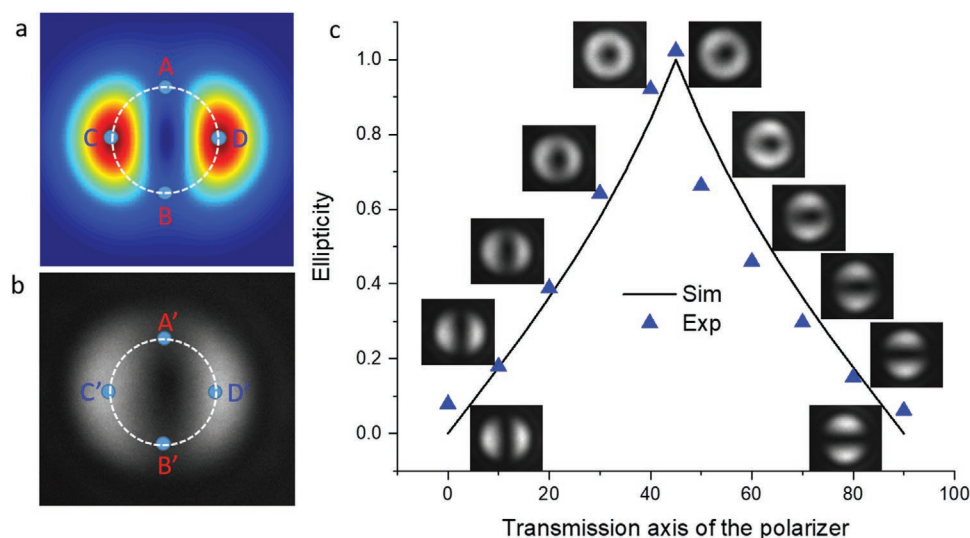


Figure 5. Ellipticity measurement based on the minimum and maximum intensities from the images. a) Simulation and b) experimental results of the intensity distribution for a typical polarization state of the incident light. The experimentally obtained intensity distribution for the superpositions of OAM states with $\ell = 1$ and $\ell = -1$ is processed using the software ImageJ. The minimum intensity spots A' and B' on the circle are denoted by $I_{A'}$ and $I_{B'}$, and the maximum intensity spots C' and D' are denoted by $I_{C'}$ and $I_{D'}$, respectively, while the corresponding intensity spots A, B, C, and D for simulated results. c) Measured and simulated ellipticity value when the transmission axis of the polarizer changes. The experimental interference patterns are given in the insets.

vertical dash lines in the first column become narrower and narrower from bottom to top, indicating that the polarization state changes from linear polarization to left elliptical polarization, and then to left circular polarization (smallest distance). In comparison with the first column, the distances between two green vertical dash lines in the second column become wider and wider from bottom to top, indicating the polarization states changes from linear polarization to right elliptical polarization and then to right circular polarization. Details on how to determine the handedness of incident polarized light are provided in Section S4 (Supporting Information).

4. Discussion

An interesting question is how to improve the accuracy of the polarization measurement based on this approach, especially the major axis of the polarization state, which can be improved by using the superpositions of OAM beam with higher topological charges. In the first experiment, there are only two petals in the interference patterns and one dark line passing through the center. More petals and dark lines can increase the measurement accuracy since the major axis can be determined by the average values of angle shift at each maximum, equivalent to multiple measurement in an experiment. To test this idea, we fabricate a sample based on the superpositions of OAM states with $\ell = 2$ and $\ell = -2$, which can generate 4 petals with 2 dark lines. Various interference patterns from the superposition of OAM beams are obtained by rotating the transmission axis of the polarizer, while the transmission axis of analyzer is fixed along the horizontal direction. **Figure 7** presents numerically calculated and experimentally observed superpositions of OAM states with $\ell = 2$ and $\ell = -2$, when the angles of the polarizer are 0° , 45° , 90° , and -45° , respectively. It is worth mentioning

that the major axis of the polarization state corresponds to double angle shift of the petals. Although we can design a single metasurface for the realization of the two different types of OAM superpositions to measure all three parameters, the metasurface must be rotated during the measurement process. Design details on multichannel metadevices are available in the reference.^[36] A power meter can be used to measure the total power of OAM beams on both sides and the power of incident light just before impinging on the metasurface. The ratio of total power on both sides to the power of the incident light is the efficiency. Efficiency analysis for the superpositions of OAM beams based on reflective metasurfaces is also available in the reference.^[36]

5. Conclusion

A facile metasurface approach is demonstrated to detect polarization state based on light's orbital angular momentum. Superposition of OAM states has provided a new tool for polarization measurement. The polarization parameters such as major axis, ellipticity and handedness are measured using compact metasurface devices. The subwavelength resolution, ultrathin nature, and the combination of OAM generation and manipulation make this technology very attractive for many research fields, including polarization imaging, optical communications, optical tweezers, and quantum sciences.

6. Experimental Section

Sample Fabrication: The reflective metasurfaces consisted of three layers: a top layer of gold nanorods, a gold ground layer, and a silicon dioxide (SiO_2) spacer layer sandwiched between them. The standard electron beam lithography was used to fabricate the designed

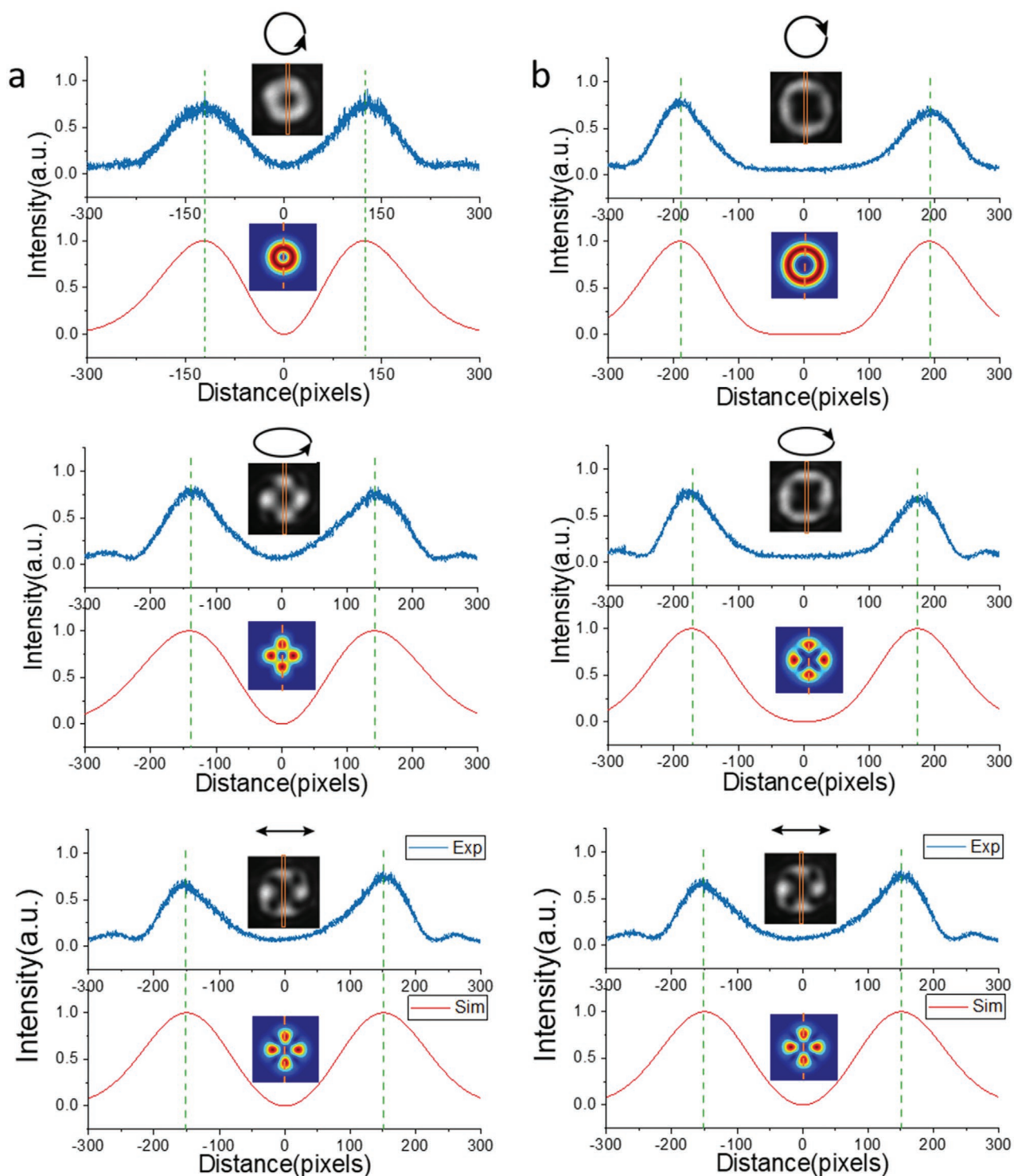


Figure 6. Handedness measurement based on the superposition of OAM beams with $\ell = 1$ and $\ell = -3$. a) The two figures at the bottom are the polarization profiles of normalized intensity for the linear polarization, and the distance between two green vertical dashed line is about 300 pixels. The distance between two green vertical dashed lines becomes narrower and narrower from bottom to top, indicating that the polarization state changes from linear polarization to left elliptical polarization, and then to left circular polarization (smallest distance). b) The distance between two green vertical dashed lines become wider and wider from bottom to top, indicating the polarization states changes from linear polarization to right elliptical polarization and then to right circular polarization. To facilitate analysis, we choose light intensity profile along a rectangle region (edge marked by the orange dashed line) with a width of 10 pixels from top to bottom passing through the center of the superposed mode based on the image processing software ImageJ). The orange dashed line in the numerical figure is the vertical center of light intensity distribution. We extract the 600×600 pixels of the center of image. The handedness of incident polarized light is determined by the distance between two peak intensities.

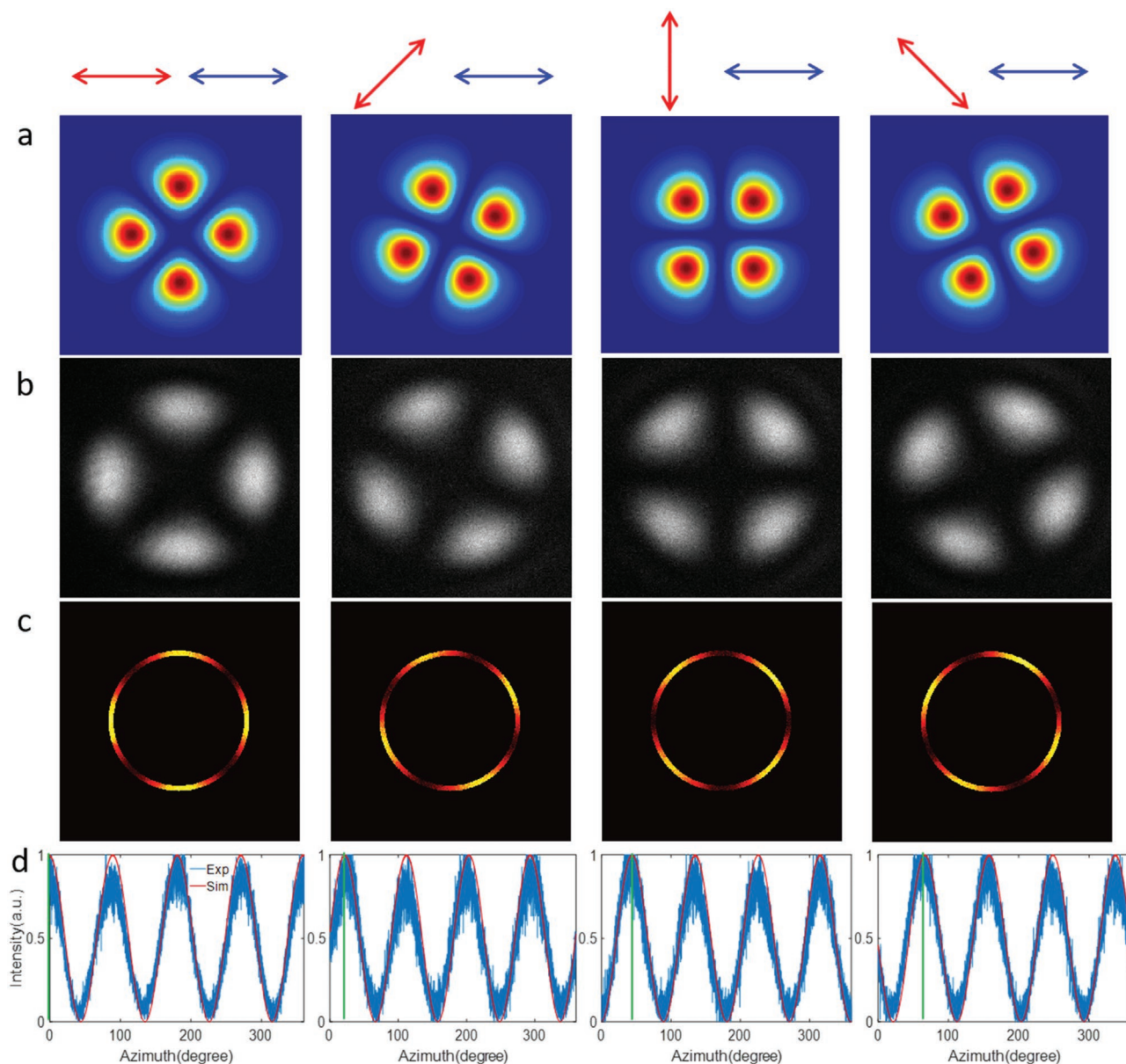


Figure 7. Major axis measurement based on superpositions of OAM states with $\ell = 2$ and $\ell = -2$. a) Simulation results for the superpositions of OAM states with $\ell = 2$ and $\ell = -2$ when the rotation angles of the polarizer are 0° , 45° , 90° , and -45° , respectively. The polarization direction of the incident linearly polarized light and the direction of the polarizer's transmission axis in front of the CCD camera are denoted by the red and blue double-headed arrows, respectively. b) Experimental results. c) The intensity distributions along the orange ring shown in Figure 3b. d) The relation between light intensity distribution in (c) and the azimuth angle.

metasurfaces, followed by film deposition and the lift-off process. First, silicon substrates were cleaned with acetone in ultrasonic bath for 10 min followed by isopropyl alcohol (IPA) for 10 min. After the substrates were ready, the gold layer (150 nm) was deposited onto the silicon substrate by using the electron beam evaporator followed by the deposition of silicon dioxide (SiO_2) layer (85 nm). The positive polymethyl methacrylate (PMMA) 950 A2 resist was spin coated on the SiO_2 layer, producing a PMMA film with a thickness of 100 nm. The nanopatterns were defined in the PMMA film using EBL (Raith PIONEER, 30 kV). The sample was developed in MIBK:IPA (1:3) for 45 s followed by stopper (IPA) for 45 s. A thin gold layer (30 nm) was deposited on the developed sample using electron beam evaporator. The reflective metasurfaces were obtained after the lift-off process in acetone.

Supporting Information

Supporting Information is available from the Wiley Online Library or from the author.

Acknowledgements

This project was supported by the Engineering and Physical Sciences Research Council of the United Kingdom (Grant Ref: EP/ P029892/1). A.M. would like to acknowledge National Natural Science Foundation of China (Grant No. 61905100) and the Fundamental Research Funds for Central Universities (Grant No. lzujbky-2020-65). Y.I. acknowledges the

support from the Ministry of Science and Technology (Thailand), and the Royal Thai Embassy in London (UK). This project was also supported by China Scholarship Council (Grant No. 201806185054, 201808535073, 201906680066).

Conflict of Interest

The authors declare no conflict of interest.

Author Contributions

A.M. and Y.I. contributed equally to this work. X.C. initiated the idea. A.M. and J.H. conducted the numerical simulations. Y.I. fabricated the sample. A.M., Y.I., J.H., and R.W. performed the measurements. A.M. and X.Z. prepared the manuscript. X.C. supervised the project. All the authors discussed and analyzed the results.

Keywords

optical metasurfaces, polarization detection, superposition of vortex beams, vortex beams

Received: March 20, 2020

Revised: May 5, 2020

Published online: June 15, 2020

- [1] J. S. Tjo, D. L. Goldstein, D. B. Chenault, J. A. Shaw, *Appl. Opt.* **2006**, *45*, 5453.
- [2] J. Bailey, A. Chrysostomou, J. H. Hough, T. M. Gledhill, A. McCall, S. Clark, F. Ménard, M. Tamura, *Science* **1998**, *281*, 672.
- [3] T. Smidlehner, I. Piantanida, G. Pescitelli, *J. Org. Chem.* **2018**, *14*, 84.
- [4] N. Ghosh, I. A. Vitkin, *J. Biomed. Opt.* **2011**, *16*, 110801.
- [5] Y. Wang, H. He, J. Chang, N. Zeng, S. Liu, M. Li, H. Ma, *Micron* **2015**, *79*, 8.
- [6] D. Wen, F. Yue, S. Kumar, Y. Ma, M. Chen, X. Ren, P. E. Kremer, B. D. Gerardot, M. R. Taghizadeh, G. S. Buller, X. Chen, *Opt. Express* **2015**, *23*, 10272.
- [7] N. Yu, P. Genevet, M. A. Kats, F. Aieta, J.-P. Tetienne, F. Capasso, Z. Gaburro, *Science* **2011**, *334*, 333.
- [8] A. V. Kildishev, A. Boltasseva, V. M. Shalaev, *Science* **2013**, *339*, 1232009.
- [9] D. Lin, P. Fan, E. Hasman, M. L. Brongersma, *Science* **2014**, *345*, 298.
- [10] X. Chen, L. Huang, H. Mühlenbernd, G. Li, B. Bai, Q. Tan, G. Jin, C. Qiu, S. Zhang, T. Zentgraf, *Nat. Commun.* **2012**, *3*, 1198.
- [11] L. Huang, X. Chen, H. Mühlenbernd, H. Zhang, S. Chen, B. Bai, Q. Tan, G. Jin, K.-W. Cheah, C. Qiu, J. Li, T. Zentgraf, S. Zhang, *Nat. Commun.* **2013**, *4*, 2808.
- [12] X. Ni, A. V. Kildishev, V. M. Shalaev, *Nat. Commun.* **2013**, *4*, 2807.
- [13] X. F. Zang, F. L. Dong, F. Y. Yue, C. M. Zhang, L. H. Xu, Z. W. Song, M. Chen, P.-Y. C., G. S. Buller, Y. M. Zhu, S. L. Zhuang, W. G. Chu, S. Zhang, X. Z. Chen, *Adv. Mater.* **2018**, *30*, 1707499.
- [14] D. Wen, F. Yue, G. Li, G. Zheng, K. Chan, S. Chen, M. Chen, K. F. Li, P. W. H. Wong, K. W. Cheah, E. Y. B. Pun, S. Zhang, X. Chen, *Nat. Commun.* **2015**, *6*, 8241.
- [15] G. Zheng, S. Zhang, G. Li, M. Kenney, H. Mühlenbernd, T. Zentgraf, *Nat. Nanotechnol.* **2015**, *10*, 308.
- [16] M. Khorasaninejad, K. B. Crozier, *Nat. Commun.* **2014**, *5*, 5386.
- [17] P. C. Wu, J.-W. Chen, C.-W. Yin, Y.-C. L., T. L. Chung, C. Y. Liao, B. H. Chen, K.-W. Lee, C.-J. Chuang, C.-M. Wang, D. P. Tsai, *ACS Photonics* **2018**, *5*, 2568.
- [18] A. Pors, M. G. Nielsen, S. I. Bozhevolnyi, *Optica* **2015**, *2*, 716.
- [19] X. Zhang, S. Yang, W. Yue, Q. Xu, C. Tian, X. Zhang, E. Plum, S. Zhang, J. Han, W. Zhang, *Optica* **2019**, *6*, 1190.
- [20] M. Khorasaninejad, W. T. Chen, A. Y. Zhu, J. Oh, R. C. Devlin, D. Rousso, F. Capasso, *Nano Lett.* **2016**, *16*, 4595.
- [21] N. A. Rubin, G. D'Aversa, P. Chevalier, Z. Shi, W. T. Chen, F. Capasso, *Science* **2019**, *365*, eaax1839.
- [22] L. Allen, M. W. Beijersbergen, R. J. C. Spreeuw, J. P. Woerdman, *Phys. Rev. A* **1992**, *45*, 8185.
- [23] P. Chen, S. J. Ge, W. Duan, B. Y. Wei, G. X. Cui, W. Hu, Y. Q. Lu, *ACS Photonics* **2017**, *4*, 1333.
- [24] M. Padgett, R. Bowman, *Nat. Photonics* **2011**, *5*, 343.
- [25] L. Torner, J. P. Torres, *Opt. Express* **2005**, *13*, 873.
- [26] Y. Bao, J. Ni, C.-W. Qiu, *Adv. Mater.* **2020**, *32*, 1905659.
- [27] L. Jin, Y. W. Huang, Z. Jin, R. C. Devlin, Z. Dong, S. Mei, W. T. Chen, Z. Wei, H. Liu, J. Teng, A. Danner, X. Li, S. Xiao, S. Zhang, C. Yu, J. K. W. Yang, F. Capasso, C. W. Qiu, *Nat. Commun.* **2019**, *10*, 4789.
- [28] K. Dholakia, N. B. Simpson, M. J. Padgett, L. Allen, *Phys. Rev. A* **1996**, *54*, R3742.
- [29] J. Courtial, K. Dholakia, L. Allen, M. J. Padgett, *Phys. Rev. A* **1997**, *56*, 4193.
- [30] A. Mair, A. Vaziri, G. Weihs, A. Zeilinger, *Nature* **2001**, *412*, 313.
- [31] S. S. R. Oemrawsingh, X. Ma, D. Voigt, A. Aiello, E. R. Eliel, G. W. 't Hooft, J. P. Woerdman, *Phys. Rev. Lett.* **2005**, *95*, 240501.
- [32] J. Leach, B. Jack, J. Romero, A. K. Jha, A. M. Yao, S. F. Arnold, D. G. Ireland, R. W. Boyd, S. M. Barnett, M. J. Padgett, *Science* **2010**, *329*, 662.
- [33] X. F. Zang, Y. M. Zhu, C. X. Mao, W. W. Xu, H. Z. Ding, J. Y. Xie, Q. Q. Cheng, L. Chen, Y. Peng, Q. Hu, M. Gu, S. L. Zhuang, *Adv. Opt. Mater.* **2019**, *7*, 1801328.
- [34] E. L. Wang, L. N. Shi, J. B. Niu, Y. L. Hua, H. L. Li, X. L. Zhu, C. Q. Xie, T. C. Ye, *Adv. Opt. Mater.* **2019**, *7*, 1801415.
- [35] L. Huang, X. Chen, H. Mühlenbernd, G. Li, B. Bai, Q. Tan, G. Jin, T. Zentgraf, S. Zhang, *Nano Lett.* **2012**, *12*, 5750.
- [36] F. Yue, D. Wen, C. Zhang, B. D. Gerardot, W. Wang, S. Zhang, X. Chen, *Adv. Mater.* **2017**, *29*, 1603838.
- [37] L. Huang, X. Chen, B. Bai, Q. Tan, G. Jin, T. Zentgraf, S. Zhang, *Light: Sci. Appl.* **2013**, *2*, e70.
- [38] F. Yue, D. Wen, J. Xin, B. D. Gerardot, J. Li, X. Chen, *ACS Photonics* **2016**, *3*, 1558.
- [39] C. Zhang, F. Yue, D. Wen, M. Chen, Z. Zhang, W. Wang, X. Chen, *ACS Photonics* **2017**, *4*, 1906.
- [40] C. Zhang, D. Wen, F. Yue, Y. Intaravanne, W. Wang, X. Chen, *Phys. Rev. Appl.* **2018**, *10*, 034028.